

# Flatness-based trajectory planning for 3D overhead cranes with friction compensation and collision avoidance.

Jorge Vicente-Martinez and Edgar Ramirez-Laboreo

**Abstract**—This paper presents an optimal trajectory generation method for 3D overhead cranes by leveraging differential flatness. This framework enables the direct inclusion of complex physical and dynamic constraints, such as nonlinear friction and collision avoidance for both payload and rope. Our approach allows for aggressive movements by constraining payload swing only at the final point. A comparative simulation study validates our approach, demonstrating that neglecting dry friction leads to actuator saturation and collisions. The results show that friction modeling is a fundamental requirement for fast and safe crane trajectories.

**Index Terms**—Mechatronic systems, 3D overhead crane, friction modeling, collision avoidance, underactuated system, differential flatness.

## I. INTRODUCTION

The lifting and transport of heavy loads are key operations in modern industrial environments like factories and ports, often performed by manually operated cranes. Trends toward optimizing processes and improving safety are driving research into the autonomous operation of this machinery, for which generating optimal, collision-free trajectories is a critical challenge. Recent works address trajectory planning for various crane types, such as the collision-free motion planning for an autonomous timber crane presented in [1], and the hook position error compensation for tower cranes studied in [2].

Among industrial cranes, overhead cranes are widely utilized in indoor and industrial zones. They face two main challenges: they are underactuated, as the rope-connected payload cannot be directly controlled, and their motion is significantly affected by friction. The influence of friction has been highlighted by several authors. For instance, [3] noted that friction effects are not negligible, even on a laboratory-scale crane. Furthermore, [4] experimentally demonstrated that the system's friction can depend on both position and direction

of motion, remarking that significant control effort is dedicated to friction compensation.

While trajectory planning for 3D overhead cranes is well-addressed in the literature by means of a variety of methods [5]–[9], a common simplification is omitting friction in the dynamic models used for trajectory optimization, likely due to the numerical challenges of modeling this phenomenon.

Another key aspect is rope-obstacle collision, which most studies neglect by assuming small payload swing angles [10]. To our knowledge, only [11] include constraints for both the payload and the rope in trajectory planning for 3D cranes with obstacles. However, this work only considers collisions of the rope with the top surface of obstacles, which is a simplification that does not capture all possible collision scenarios. This approach, which focuses on minimizing payload swing throughout the trajectory, can limit the time and energy optimality of the resulting paths by not exploiting the full range of possible motions. In other fields, such as the control of unmanned aerial vehicles (UAVs) with suspended loads, the problem of rope collision with obstacles has been more thoroughly addressed, as demonstrated in works like [12] and [13].

To address these challenges, this paper focuses on optimal trajectory planning for 3D overhead cranes. We propose a method for generating trajectories that ensures both the payload and the rope are collision-free, while only requiring the payload oscillations to be minimized at the final point. This allows for more time and energy-efficient trajectories by leveraging the natural dynamics of the system. Exploiting the properties of differential flatness on overhead cranes, we incorporate for the first time a complex dry friction model into the trajectory planning framework. We present a comparative analysis of the trajectories generated using three different friction models of varying complexity—a complete model, a simplified model, and a no dry friction model—and evaluate their performance in a high-fidelity simulator.

## II. SYSTEM DYNAMICS

### A. Equations of Motion

The three-dimensional overhead crane under consideration is depicted schematically in Fig. 1. The system consists of a rail of mass  $m_r$  that travels along the X-axis and a trolley of mass  $m_t$  mounted on the rail, which moves along the Y-axis. A payload, modeled as a point mass  $m_p$  is suspended from the

This work was supported in part via grants PID2021-124137OB-I00 and PID2024-159279OB-I00, funded by MCIN/AEI/10.13039/501100011033 and by ERDF A way of making Europe, and in part by the Government of Aragón - EU, under grant T45\_23R and predoctoral researcher contract of J.Vicente. (Corresponding author: J. Vicente-Martinez.)

The authors are with the Departamento de Informatica e Ingenieria de Sistemas (DIIS) and the Instituto de Investigacion en Ingenieria de Aragon (I3A), Universidad de Zaragoza, 50018 Zaragoza, Spain (e-mail: j.vicente@unizar.es; ramirlab@unizar.es).

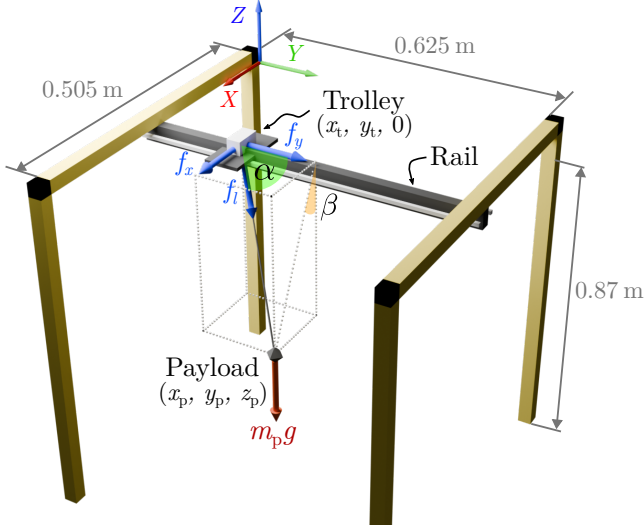


Fig. 1. Schematic diagram of the overhead crane.

trolley by a rigid rope of variable length. The configuration of the system is described by five generalized coordinates: the Cartesian position of the trolley  $(x_t, y_t)$ , the rope length  $L$ , and the two swing angles,  $\alpha$  and  $\beta$ . The crane is actuated by three control forces:  $f_x$  applied to the rail,  $f_y$  to the trolley, and  $f_l$  to the hoisting mechanism.

The model incorporates friction forces that oppose motion in each actuated axis. The friction in the X and Y axes is modeled as position- and velocity-dependent functions,  $d_x(x_t, \dot{x}_t)$  and  $d_y(y_t, \dot{y}_t)$ , while the rope axis friction,  $d_l(\dot{L})$ , depends only on velocity.

The dynamic model of the crane is derived using the Euler-Lagrange formulation. Following the model presented in our previous work [14], the equations of motion are given by:

$$\ddot{x}_t = \frac{f_x - d_x(x_t, \dot{x}_t) - (f_l - d_l(\dot{L})) \sin \alpha \sin \beta}{J_x + m_t + m_r}, \quad (1)$$

$$\ddot{y}_t = \frac{f_y - d_y(y_t, \dot{y}_t) - (f_l - d_l(\dot{L})) \cos \alpha}{J_y + m_t}, \quad (2)$$

$$\begin{aligned} \ddot{L} = & (f_l - d_l(\dot{L}) - m_p \cos \alpha \ddot{y}_t + m_p L \dot{\alpha}^2 \\ & + m_p L \dot{\beta}^2 - m_p \cos^2 \alpha L \dot{\beta}^2 - m_p \sin \alpha \sin \beta \ddot{x}_t \\ & + g m_p \cos \beta \sin \alpha) / (m_p + J_l), \end{aligned} \quad (3)$$

$$\begin{aligned} \ddot{\alpha} = & (\sin \alpha \ddot{y}_t - \cos \alpha \sin \beta \ddot{x}_t + g \cos \alpha \cos \beta \\ & + \cos \alpha \sin \alpha L \dot{\beta}^2 - 2 \dot{L} \dot{\alpha}) / L, \end{aligned} \quad (4)$$

$$\ddot{\beta} = \frac{-g \sin \beta - \cos \beta \ddot{x}_t - 2 \sin \alpha \dot{L} \dot{\beta} - 2 \cos \alpha L \dot{\alpha} \dot{\beta}}{\sin \alpha L}, \quad (5)$$

where  $g$  is the acceleration due to gravity, and  $J_x, J_y, J_l$  are the effective inertia-related parameters for the X, Y, and rope axes, respectively.

## B. Friction Model

A key aspect of this work is the inclusion of a detailed friction model. As established in the previously cited publication, friction in the trolley's motion axes can depend on both position and velocity direction. The effective friction force in each axis is modeled as the sum of a viscous friction term and a dry (Coulomb) friction term. For the X-axis (and equivalently for the Y-axis, with its own parameters), the effective friction can be expressed as

$$d_x(x_t, \dot{x}_t) = D_x(\dot{x}_t) \dot{x}_t + C_x(x_t, \dot{x}_t), \quad (6)$$

where the direction-dependent viscous friction for the X-axis,  $D_x(\dot{x}_t)$ , is defined as a piecewise function:

$$D_x(\dot{x}_t) = \begin{cases} D_x^{(-)} & \text{if } \dot{x}_t < 0 \\ 0 & \text{if } \dot{x}_t = 0 \\ D_x^{(+)} & \text{if } \dot{x}_t > 0 \end{cases}, \quad (7)$$

where  $D_x^{(-)}$  and  $D_x^{(+)}$  are the effective viscous friction coefficients for each direction of movement. Similarly, the effective dry friction term,  $C_x(x_t, \dot{x}_t)$ , is dependent on both position and direction:

$$C_x(x_t, \dot{x}_t) = \begin{cases} C_x^{(-)}(x_t) & \text{if } \dot{x}_t < 0 \\ 0 & \text{if } \dot{x}_t = 0 \\ C_x^{(+)}(x_t) & \text{if } \dot{x}_t > 0 \end{cases}, \quad (8)$$

where the functions  $C_x^{(-)}(x_t)$  and  $C_x^{(+)}(x_t)$  are modeled in this case as fourth-order polynomials:

$$C_x^{(-)}(x_t) = a_{x0} + a_{x1}x_t + a_{x2}x_t^2 + a_{x3}x_t^3 + a_{x4}x_t^4, \quad (9)$$

$$C_x^{(+)}(x_t) = b_{x0} + b_{x1}x_t + b_{x2}x_t^2 + b_{x3}x_t^3 + b_{x4}x_t^4, \quad (10)$$

where the coefficients  $a_{xi}$  and  $b_{xi}$  for  $i \in \{0, \dots, 4\}$  are constant parameters estimated from data. For the rope-hoisting axis, mechanical friction is considered negligible, and the model only accounts for motor-related effects:

$$d_l(\dot{L}) = D_l \dot{L} + C_l \text{sign}(\dot{L}), \quad (11)$$

where  $D_l$  and  $C_l$  are, respectively, the constant effective viscous and dry friction coefficients for the hoist axis.

## C. Differential Flatness

The overhead crane is a flat system and the position of the payload,  $\mathbf{r}_p = [x_p, y_p, z_p]^T$ , is a flat output [15]. This implies that all system states,  $\mathbf{x} = [x_t, \dot{x}_t, y_t, \dot{y}_t, L, \dot{L}, \alpha, \dot{\alpha}, \beta, \dot{\beta}]^T$ , and control inputs,  $\mathbf{u} = [f_x, f_y, f_l]^T$ , can be expressed analytically as functions of the flat output and a finite number of its time derivatives. The relationships between the system's generalized coordinates and the flat output are given by the following inverse dynamics mapping:

$$x_t = x_p - L \sin \beta \sin \alpha, \quad (12)$$

$$y_t = y_p - L \cos \alpha, \quad (13)$$

$$L = -z_p / (\sin \alpha \cos \beta), \quad (14)$$

$$\alpha = \arctan \left( -\sqrt{\ddot{x}_p + (\ddot{z}_p + g)^2 / \ddot{y}_p} \right), \quad (15)$$

$$\beta = \arctan (\ddot{x}_p / (-\ddot{z}_p - g)). \quad (16)$$

The control input can be obtained by successively differentiating (12)–(16) and substituting the results into the equations of motion (1)–(5). This yields a set of functions that map the payload trajectory to the required actuator forces, even in the presence of the complex, state-dependent friction model. In other words,  $\mathbf{u}$  can be expressed as

$$\mathbf{u} = \psi \left( \mathbf{r}_p, \dot{\mathbf{r}}_p, \ddot{\mathbf{r}}_p, \mathbf{r}_p^{(3)}, \mathbf{r}_p^{(4)}, \boldsymbol{\theta} \right), \quad (17)$$

where  $\psi$  is the vector-valued mapping function, and  $\boldsymbol{\theta}$  is the vector of system parameters, including masses, inertia, and friction coefficients.

The principal advantage of leveraging differential flatness is the transformation of the complex nonlinear dynamics into a simple, linear time-invariant (LTI) representation where the trajectories can be planned directly on the payload and its time derivatives. Various authors in the literature have taken advantage of this property to generate trajectories and different control strategies for 3D overhead cranes, such as [16], [10] and [17].

The system dynamics can then be expressed as a chain of integrators by defining the new input as the fourth derivative of the flat output,  $\bar{\mathbf{u}} = \mathbf{r}_p^{(4)}$ :

$$\dot{\bar{\mathbf{x}}}(t) = \mathbf{A}\bar{\mathbf{x}}(t) + \mathbf{B}\bar{\mathbf{u}}(t), \quad (18)$$

where

$$\bar{\mathbf{x}} = \left[ x_p, \dot{x}_p, \ddot{x}_p, x_p^{(3)}, y_p, \dot{y}_p, \ddot{y}_p, y_p^{(3)}, z_p, \dot{z}_p, \ddot{z}_p, z_p^{(3)} \right]^T, \quad (19)$$

and the state and input matrices,  $\mathbf{A} \in \mathbb{R}^{12 \times 12}$  and  $\mathbf{B} \in \mathbb{R}^{12 \times 3}$  are given by

$$\mathbf{A} = \mathbf{I}_3 \otimes \begin{bmatrix} 0 & 1 & 0 & 0 \\ 0 & 0 & 1 & 0 \\ 0 & 0 & 0 & 1 \\ 0 & 0 & 0 & 0 \end{bmatrix}, \quad \mathbf{B} = \mathbf{I}_3 \otimes \begin{bmatrix} 0 \\ 0 \\ 0 \\ 1 \end{bmatrix}, \quad (20)$$

where  $\otimes$  denotes the Kronecker product and  $\mathbf{I}_3$  is the  $3 \times 3$  identity matrix.

### III. TRAJECTORY OPTIMIZATION PROBLEM

Using the flat system representation of the overhead crane dynamics, the goal is to guide the system from an initial state  $\bar{\mathbf{x}}_{\text{START}}$  to a final state  $\bar{\mathbf{x}}_{\text{END}}$  while satisfying all mechanical and obstacle-related constraints.

#### A. Physical Constraints

To ensure that the generated trajectories are physically feasible, the following constraints are considered, all of which must be satisfied throughout the entire trajectory, i.e., for all  $t \in [0, T_{\text{END}}]$ , where  $T_{\text{END}}$  is the final time.

1) *Trolley position and rope length limits*: The crane's operational workspace is bounded by the physical travel limits of the trolley and rail. Additionally, the rope has minimum and maximum extension limits. These are formulated as box constraints:

$$x_{\text{MIN}} \leq x_i(t) \leq x_{\text{MAX}}, \quad (21)$$

$$y_{\text{MIN}} \leq y_i(t) \leq y_{\text{MAX}}, \quad (22)$$

$$L_{\text{MIN}} \leq L(t) \leq L_{\text{MAX}}, \quad (23)$$

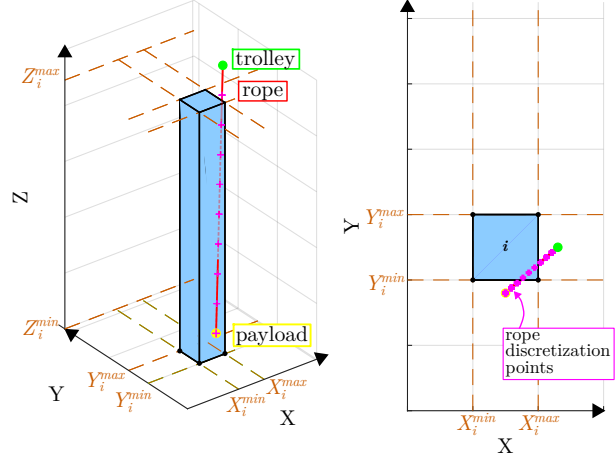


Fig. 2. Parameterization of the  $i$ -th obstacle model and visualization of the collision avoidance strategy.

where the subscripts  $\text{MIN}$  and  $\text{MAX}$  denote the lower and upper bounds for each respective variable. These variables are obtained at each time from the state vector  $\bar{\mathbf{x}}(t)$  using the inverse dynamics mapping (12)–(16).

2) *Actuator Saturation*: The control forces applied to the system are limited, hence, the following constraints are imposed:

$$\mathbf{u}_{\text{MIN}} \leq \mathbf{u}(t) \leq \mathbf{u}_{\text{MAX}}, \quad (24)$$

where  $\mathbf{u}_{\text{MIN}}$  and  $\mathbf{u}_{\text{MAX}}$  are the vectors containing the minimum and maximum values of each input force. The input  $\mathbf{u}$  is computed from  $\bar{\mathbf{x}}$  and  $\bar{\mathbf{u}} = \mathbf{r}_p^{(4)}$  via (17).

#### B. Obstacle Avoidance

In this work, we consider the potential collisions between both the payload and the rope with a set of  $N_b$  static obstacles where the  $i$ -th obstacle is modeled as a rectangular prism defined by its boundary limits  $X_i^{\text{min}}, X_i^{\text{max}}, Y_i^{\text{min}}, Y_i^{\text{max}}, Z_i^{\text{min}}, Z_i^{\text{max}}$  (see Fig. 2).

Looking for computational efficiency, we use a sampling-based approach for rope-obstacle collision checking, as depicted in Fig. 2. At each time, the rope segment connecting the trolley  $\mathbf{r}_t = [x_t, y_t, 0]^T$  and the payload  $\mathbf{r}_p$  is discretized into  $N_r$  equidistant points,  $\mathbf{r}_{rj} = [x_{rj}, y_{rj}, z_{rj}]$ , for  $j = 1, \dots, N_r$ , where

$$\mathbf{r}_{rj}(t) = \frac{N_r - j}{N_r - 1} \mathbf{r}_t(t) + \frac{j - 1}{N_r - 1} \mathbf{r}_p(t). \quad (25)$$

To evaluate potential intersections between the rope point  $\mathbf{r}_{rj}$  and the  $i$ -th obstacle, we define a constraint function  $\varphi_{ji}(\bar{\mathbf{x}})$ . This function ensures that the distance from the point to the obstacle is greater than or equal to a safety margin  $\varepsilon$ :

$$\varphi_{ji}(\bar{\mathbf{x}}(t)) = \|\mathbf{d}_{ji}(\bar{\mathbf{x}}(t))\|_2 - \varepsilon \geq 0, \quad (26)$$

where  $\mathbf{d}_{ji}(\bar{\mathbf{x}})$  is the vector of minimum distances from the point to the interior of the obstacle along each axis:

$$\mathbf{d}_{ji}(\bar{\mathbf{x}}) = \begin{bmatrix} \max(0, X_i^{\text{min}} - x_{rj}, x_{rj} - X_i^{\text{max}}) \\ \max(0, Y_i^{\text{min}} - y_{rj}, y_{rj} - Y_i^{\text{max}}) \\ \max(0, Z_i^{\text{min}} - z_{rj}, z_{rj} - Z_i^{\text{max}}) \end{bmatrix}. \quad (27)$$

### C. Complete Optimization Problem

The primary objective is to find the time-optimal trajectory, which corresponds to minimizing the final time  $T_{\text{END}}$ . However, to ensure smooth and dynamically feasible motions, a secondary objective is included to penalize the squared magnitude of the snap—the fourth derivative of the position—, a technique widely used to generate minimum-snap trajectories [18]. The optimization problem to be solved is:

$$\begin{aligned} & \underset{\bar{\mathbf{x}}(t), \bar{\mathbf{u}}(t), T_{\text{END}}}{\text{minimize}} && T_{\text{END}} + \lambda \int_0^{T_{\text{END}}} \|\mathbf{r}_p^{(4)}(t)\|^2 dt \quad (28) \\ & \text{subject to} && \dot{\bar{\mathbf{x}}}(t) = \mathbf{A}\bar{\mathbf{x}}(t) + \mathbf{B}\bar{\mathbf{u}}(t) \\ & && \bar{\mathbf{x}}(0) = \bar{\mathbf{x}}_{\text{START}} \\ & && \bar{\mathbf{x}}(T_{\text{END}}) = \bar{\mathbf{x}}_{\text{END}} \\ & && \bar{\mathbf{u}}(T_{\text{END}}) = \bar{\mathbf{u}}_{\text{END}} \\ & && x_{t\text{MIN}} \leq x_t(t) \leq x_{t\text{MAX}} \\ & && y_{t\text{MIN}} \leq y_t(t) \leq y_{t\text{MAX}} \\ & && L_{\text{MIN}} \leq L(t) \leq L_{\text{MAX}} \\ & && \mathbf{u}_{\text{MIN}} \leq \mathbf{u}(t) \leq \mathbf{u}_{\text{MAX}} \\ & && \varphi_{ji}(\bar{\mathbf{x}}(t)) \geq 0 \\ & && j = 1, \dots, N_r, \quad i = 1, \dots, N_b, \end{aligned}$$

where  $\lambda$  is a weighting parameter that balances time optimality against trajectory smoothness.

This nonlinear programming problem (NLP) has been implemented using a direct collocation method, where the trajectory has been discretized into  $N_c$  intervals defined by  $N_c + 1$  collocation points [19]. The continuous-time dynamics (18) has been discretized by 4th-order Runge-Kutta integrator with a time step  $\Delta t = T_{\text{END}}/N_c$ . The complete nonlinear optimization problem has been implemented in CasADi [20] and solved using IPOPT [21]. While this method guarantees finding a minimum, the problem is rendered non-convex by obstacle avoidance and other nonlinear constraints, so global optimality cannot be assured. From an engineering perspective, however, the primary objective is thus to efficiently compute a dynamically feasible and safe trajectory, rather than to prove global optimality.

### D. Initial Guess

As stated, the trajectory optimization problem described is non-convex, making the solver's performance highly sensitive to the initial guess. To mitigate this, we employ a two-stage strategy, commonly used in motion planning [22]. First, a geometrically feasible path for the payload is generated using an asymptotically optimal sampling-based planner, RRT\* [23]. This planner finds a collision-free path from the start to the end point without considering system dynamics. The resulting path, composed of discrete waypoints, is then converted into a smooth, sufficiently differentiable trajectory using polynomial splines, which serves as the initial guess for the nonlinear optimization problem. Fig. 3 shows an illustrative case with the initial guess generated by this method alongside the final, optimized trajectory with the complete model for both the trolley and the payload.

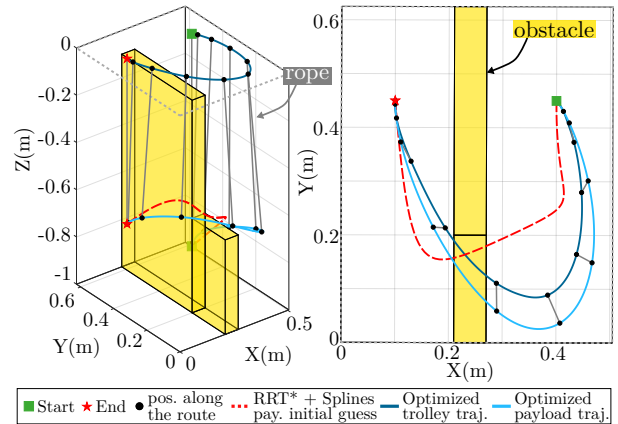


Fig. 3. Example of the trajectory optimization process. The figure shows the initial guess, and the final optimized trajectories for the trolley and the payload.

## IV. SIMULATION RESULTS

This section presents a comparative study to demonstrate the importance of friction model fidelity in trajectory optimization. The influence of the model used for planning is evaluated based on three key indicators: the presence of collisions, the final trajectory time and the residual payload oscillation, which is quantified as the maximum displacement of the payload from its final resting position after the trolley stops. The primary operational goal is to achieve zero final swing without collisions during the path, a key requirement for safe crane operation. To this end, starting from the same calculated initial guess, we compare the trajectories generated using three dynamic models of varying complexity. The two simpler models are representative of those most widely used in the literature:

- **Complete Model (CM).** The most accurate representation, incorporating the full friction dynamics detailed in Section II.
- **Simplified Model (SM).** This model replaces the direction-dependent friction terms with single constant coefficients for each axis.
- **No Dry Friction Model (NFM).** The simplest model, which entirely neglects dry friction and only includes the averaged viscous friction terms from the Simplified Model.

### A. Simulation Setup

To compare the performance of the different models, two trajectories are generated and validated using Crane3DSim [14], a high-fidelity simulator that implements the complete, position- and direction-dependent friction model. A sampling time of  $\Delta t = 0.01$  s and a snap cost weight of  $\lambda = 0.001$ , empirically found to provide a good balance between time optimality and smoothness, were used for all optimization problems.

Typically, in industrial environments, only the trolley's position and the rope length are controlled. For that reason, the optimized flat output trajectories are mapped to generate the

target paths for the actuated coordinates and the corresponding feedforward control action,  $\mathbf{u}_{ff}$ . It could be argued that a sufficiently advanced feedback controller could compensate for inaccuracies from a simplified optimization model. However, in this paper we want to demonstrate that relying on feedback is in many cases not sufficient to correct unmodeled dynamics caused by friction. To test this hypothesis, we implement a control strategy that combines the optimized feedforward action with a standard feedback term,  $\mathbf{u}_{fb}$ . We employ a conventional feedback structure: three independent PI controllers with anti-windup, one for each actuated axis, which track the specified target paths for the trolley and rope. To isolate the effects of the friction model, the PI parameters for each test case are individually tuned to minimize the sum of the Integrals of Absolute Error (IAE) of the trolley position and rope length for the trajectory generated with the simplest model (NFM). This ensures that the feedback controller is consistently optimized and that performance differences can be attributed primarily to the optimization trajectory and control plan.

Two scenarios with different obstacle layouts have been considered to evaluate the performance of each model, both designed so that the load moves on all directions. While the viscous friction coefficients are known and constant across all models [14], the dry friction functions for the simulator are generated randomly within realistic bounds to represent a plausible real-world system. A safety margin on obstacle avoidance of  $\varepsilon = 0.01$  m is used in all cases.

### B. Collision analysis along the path

First, we evaluate the performance of the trajectories under nominal conditions, where the simulator's friction parameters exactly match those of the Complete Model. The results for Scenario 1, which requires moving the payload over an obstacle, are presented in Figs. 4–6. For friction-aware models (CM and SM), the optimized trajectory for the load is realistic, ensuring the actually applied action closely matches the planned action (see Fig. 5). Consequently, both the trolley and the load move as planned. In contrast, the NFM computes an overly aggressive trajectory that underestimates the true required control effort. When this plan is simulated, the feedback controller's attempt to compensate for the unmodeled friction leads to prolonged actuator saturation, resulting in the rope not reaching the planned length (see Fig. 6) and in the application of unplanned forces on the load. As a result, the payload cannot follow the planned trajectory with errors up to 0.0327 m, calculated as the Euclidean distance between the planned and the simulated payload positions. These errors ultimately cause the payload to collide with the obstacles, as shown in the last plot of Fig. 4.

Scenario 2 consists of three obstacles that the payload must navigate between and pass over in order to find the best path. The results, shown in Figs. 7–8, are similar to those in Scenario 1. Although the action applied to the X and Y axes is corrected by the feedback control, it never reaches saturation. Consequently, the position of the trolley achieved is very similar to the planned position. As in the previous case,

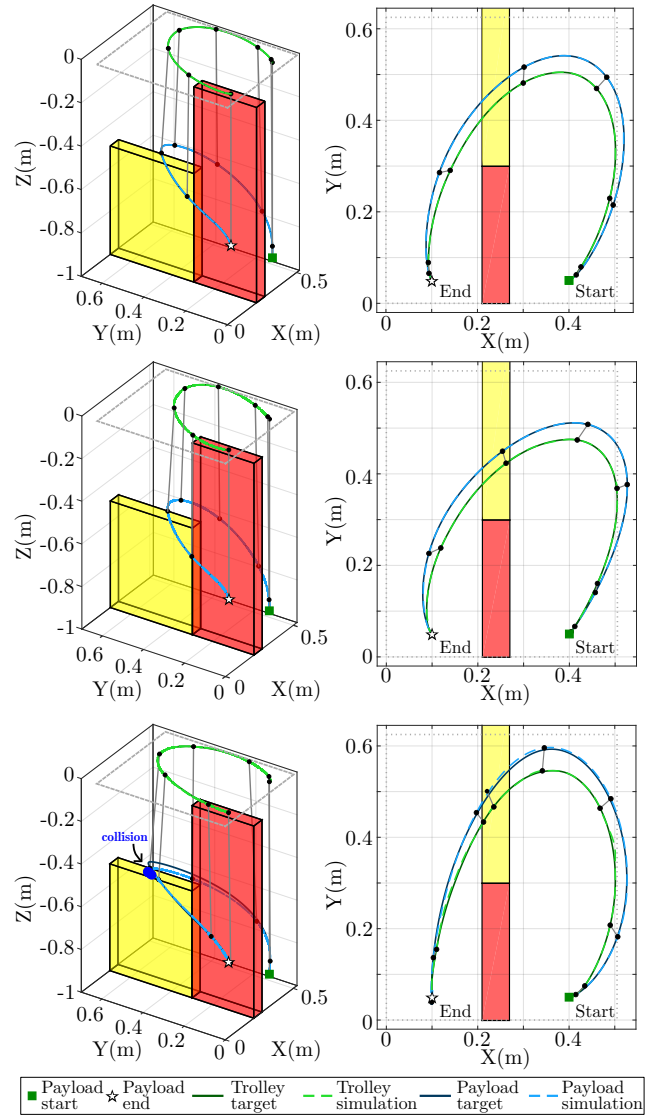


Fig. 4. Planned (target) vs. simulated trajectories for Scenario 1. Each row corresponds to a model: Complete (top), Simplified (middle), and No Dry Friction (bottom)

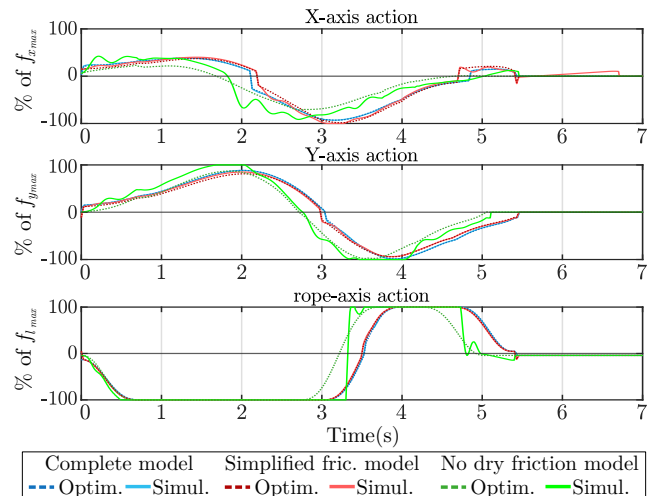


Fig. 5. Trajectory generated on optimization ( $\mathbf{u}_{ff}$ ) and simulated ( $\mathbf{u}_{ff} + \mathbf{u}_{fb}$ ) comparison for Scenario 1.

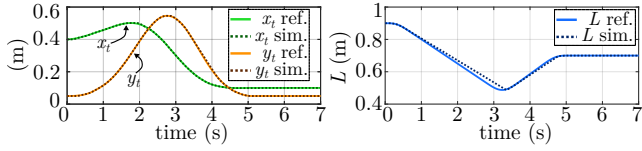


Fig. 6. Planned vs. simulated trolley position and rope for NFM nominal performance analysis.

the planned action for the rope length is insufficient to reach the target positions. This requires a correction by the feedback term that saturates the actuator and applies unplanned forces to the payload, causing errors of up to 0.0224 m and collisions with the obstacles.

### C. Trajectory Time and Payload Oscillation Analysis with Friction Uncertainty

In the following, we analyze the final trajectory time and final residual oscillations for the three models. Additionally, we conduct an analysis to assess the robustness of each model to parametric uncertainty on dry friction. We analyze whether a model incorporating friction remains superior even when its parameters do not perfectly match the true values. For that, we have performed 75 simulations for each planned trajectory, where in each run, the simulator’s dry friction parameters are perturbed with incrementally random noise, with a variation from 2% to 150% of their nominal values. Fig. 9 shows the family of randomly generated friction profiles used in Scenario 1, which are representative of those used in Scenario 2 as well. The plots show the nominal friction function from the Complete Model (solid black line) in contrast with the constant coefficient used in the Simplified Model (dotted grey line).

For a correct interpretation of the following results, it is crucial to consider the occurrence of collisions. A high rate of collisions was observed, particularly for the Simplified Model (SM), while for the other models, collision rates only became significant for friction uncertainties above 100%. However, since the simulator does not model any reaction forces resulting from these impacts, the trajectory data remains continuous. Therefore, all simulations, regardless of whether a collision occurred, are included in the following performance metrics.

Figs. 10–11 present the two analyzed indicators for these simulations on both scenarios. The first one shows the evolution of the stop time as friction uncertainty increases. Similarly, the second one illustrates the residual payload oscillation at the final time. Both analyses present a boxplot summarizing the results up to a 100% variation. The analysis shows that for the stop time, no single model offers a consistent advantage, as performance appears to be scenario-dependent. Regarding residual oscillation, however, the friction-aware models (CM and SM) demonstrate a clear advantage over the NFM. This superiority is maintained up to approximately 100% uncertainty, with the NFM’s median oscillation more than double that of the other models. This highlights that even an imperfect friction model is substantially better than neglecting dry friction entirely.

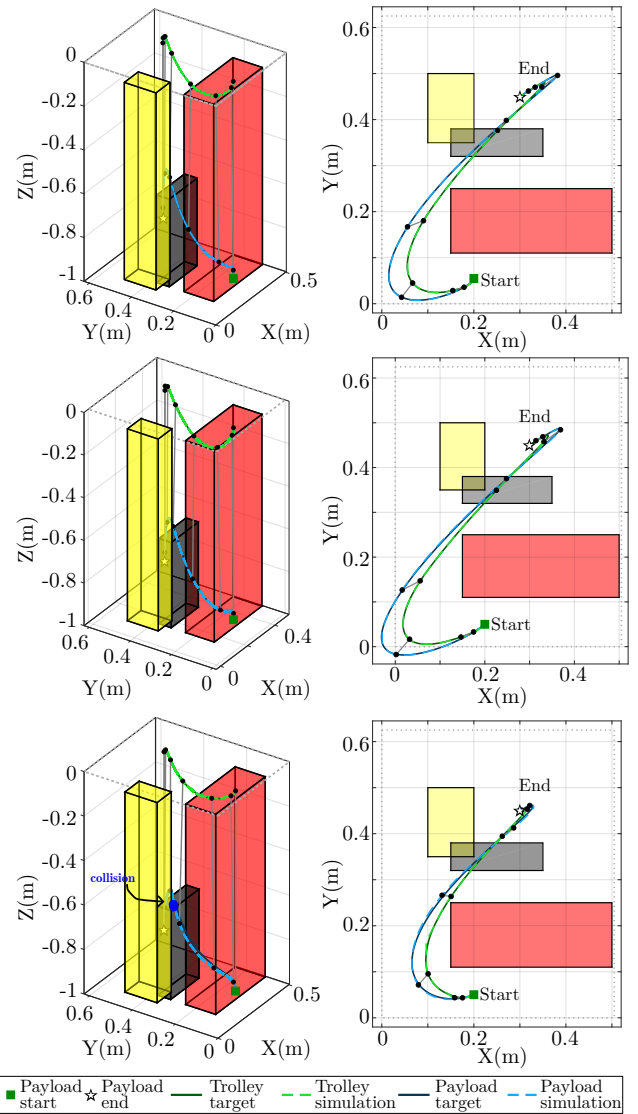


Fig. 7. Planned (target) vs. simulated trajectories for Scenario 2. Each row corresponds to a model: Complete (top), Simplified (middle), and No Dry Friction (bottom)

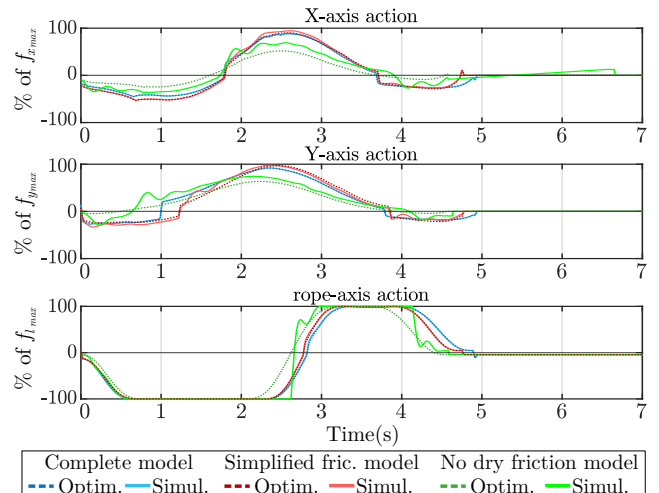


Fig. 8. Trajectory generated on optimization ( $u_{ff}$ ) and simulated ( $u_{ff} + u_{fb}$ ) comparison for Scenario 2.

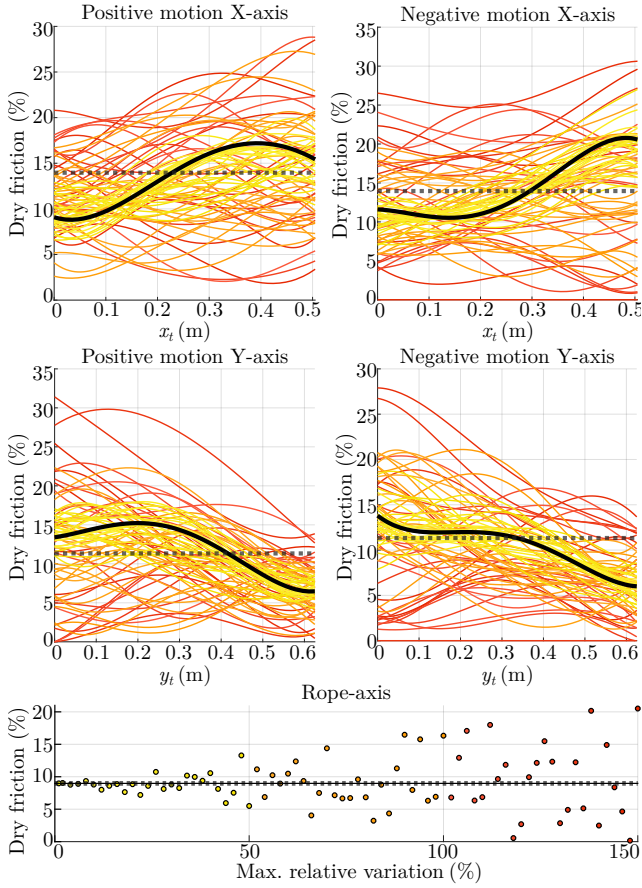


Fig. 9. Randomly generated dry friction profiles for the robustness analysis in Scenario 1. The nominal function (solid black) and the simplified coefficient (dotted grey) are shown for reference.

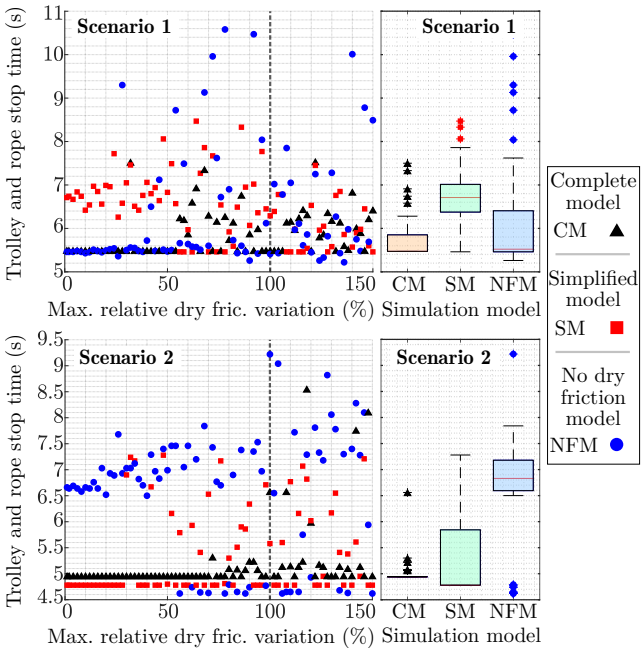


Fig. 10. Analysis of the stopping time of the trolley and rope with respect to the variation in dry friction for the three models in the two scenarios. The boxplots (right) aggregate results up to 100% uncertainty.

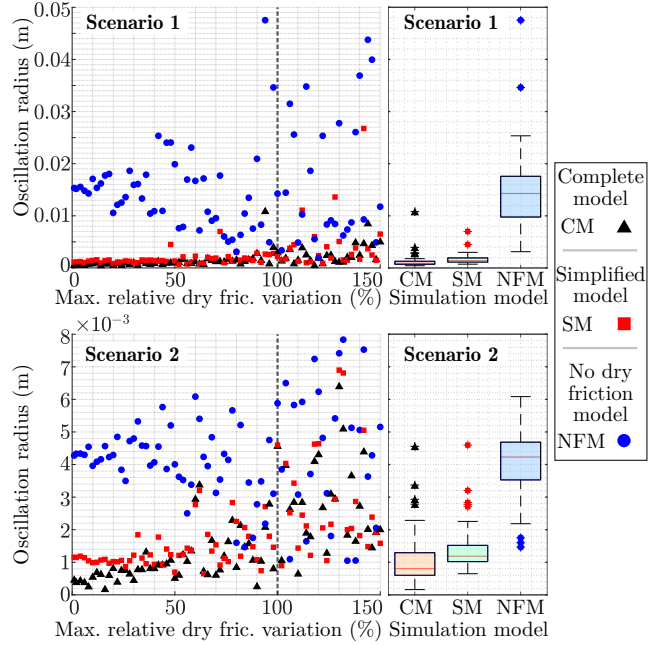


Fig. 11. Analysis of the residual payload oscillation at stop time with respect to the variation in dry friction for the three models in the two scenarios. The boxplots (right) aggregate results up to 100% uncertainty.

## V. CONCLUSIONS

In this paper, we presented a methodology to generate optimal, collision-free trajectories for 3D cranes by incorporating a high-fidelity friction model. Leveraging differential flatness, we integrated this model into the optimization, obtaining the target trajectory and a feedforward control term, allowing for aggressive movements not possible with feedback-only systems. Our approach differs from most of the existing literature by limiting oscillations only at the end point, which enables faster trajectories. This freedom of movement introduces the critical challenge of rope-obstacle collisions, which we addressed with an efficient, discretization-based constraint.

To demonstrate the advantage of including friction in optimization, two scenarios with optimized trajectories for different models were shown, using friction models with varying degrees of accuracy. The results have shown that not taking into account any dry friction term can cause the feedback term, which can only control the trolley position and the rope's length with information about those measures, to be unable to avoid obstacles in the path previously planned for the cart and rope, resulting in a collision.

Furthermore, a robustness analysis with up to 150% uncertainty in the dry friction parameters confirmed the superiority of friction-aware models with uncertainty up to 100%. While plans generated without a friction model sometimes resulted in shorter trajectory times, they consistently produced large residual oscillations when applied to the system with friction. In contrast, the friction-aware models generated more realistic feedforward plans that required minimal feedback intervention. This resulted in slightly longer trajectories in some cases, but safer with minimal final swing. Regarding the use of complex versus simplified models, it has been found

that, when a good estimate of dry friction is available, the complex model is preferable. However, accurately modeling dry friction can be difficult, so using a simplified model for dry and viscous friction also yields good results in terms of travel time and oscillation at the end of travel.

Future work will focus on the experimental validation of this methodology on a real-world laboratory crane to verify its performance and practical applicability.

## DECLARATION OF GENERATIVE AI AND AI-ASSISTED TECHNOLOGIES IN THE WRITING PROCESS

During the preparation of this work the authors used GEMINI in order to improve language. After using this tool, the authors reviewed and edited the content as needed and takes full responsibility for the content of the publication.

### REFERENCES

- [1] M.-P. Ecker, B. Bischof, M. N. Vu, C. Fröhlich, T. Glück, and W. Kemmettmüller, "Global kinodynamic motion planning for an underactuated timber crane with stochastic trajectory optimization," *Mechatronics*, vol. 108, p. 103319, Jun. 2025.
- [2] M. Burkhardt, A. Gienger, L. Joachim, N. Haala, U. Sörgel, and O. Sawodny, "Data-based error compensation for georeferenced payload path tracking of automated tower cranes," *Mechatronics*, vol. 94, p. 103028, Oct. 2023.
- [3] B. Kolar and K. Schlacher, "Flatness based Control of a Gantry Crane," *IFAC Proc. Volumes*, vol. 46, no. 23, pp. 487–492, 2013.
- [4] A. Lobe, A. Ettl, A. Steinboeck, and A. Kugi, "Flatness-based nonlinear control of a three-dimensional gantry crane," *IFAC-PapersOnLine*, vol. 51, no. 22, pp. 331–336, 2018.
- [5] S. Iftikhar, O. J. Faqir, and E. C. Kemgan, "Nonlinear model predictive control of an overhead laboratory-scale gantry crane with obstacle avoidance," in *Proc. IEEE Conf. Control Technol. Appl.* Hong Kong, China: IEEE, Aug. 2019, pp. 382–387.
- [6] V. C. Nguyen, H. L. Thi, H. B. T. Khanh, H. N. Danh, D. P. Duc, and T. L. Nguyen, "An integrated solution for 3D overhead cranes: Time-optimal motion planning, obstacle avoidance, and anti-swing," *Eng. Sci. Technol. Int. J.*, vol. 59, p. 101852, Nov. 2024.
- [7] K. Matsusawa, Y. Noda, and A. Kaneshige, "On-demand Trajectory Planning with Load Sway Suppression and Obstacles Avoidance in Automated Overhead Traveling Crane System," in *Proc. IEEE Int. Conf. Autom. Sci. Eng.* Vancouver, BC, Canada: IEEE, Aug. 2019, pp. 1321–1326.
- [8] Z. Wang, X. Cao, X. Wang, D. Wang, and J. Chen, "A Path Planning Method For Overhead Crane Based on Spatial Stratification," in *Proc. 8th Int. Conf. Control, Mech. Autom.* Moscow, Russia: IEEE, Nov. 2020, pp. 47–51.
- [9] A. Kaneshige, S. Nagai, S. Ueki, T. Miyoshi, and K. Terashima, "An algorithm for on-line path planning of autonomous mobile overhead traveling crane based on obstacle information," in *Proc. IEEE Int. Conf. Autom. Sci. Eng.* Seoul, Korea (South): IEEE, Aug. 2012, pp. 914–919.
- [10] M. Vu, M. Schwegel, C. Hartl-Nesic, and A. Kugi, "Sampling-based trajectory (re)planning for differentially flat systems: Application to a 3D gantry crane," *IFAC-PapersOnLine*, vol. 55, no. 38, pp. 33–40, 2022.
- [11] X. Wang, J. Liu, X. Dong, H. Peng, and C. Li, "An energy-time optimal autonomous motion control framework for overhead cranes in the presence of obstacles," *Proc. Inst. Mech. Eng., Part C: J. Mech. Eng. Sci.*, vol. 235, no. 13, Jul. 2021.
- [12] J. Zeng, P. Kotaru, M. W. Mueller, and K. Sreenath, "Differential Flatness Based Path Planning With Direct Collocation on Hybrid Modes for a Quadrotor With a Cable-Suspended Payload," *IEEE Robot. Autom. Lett.*, vol. 5, no. 2, pp. 3074–3081, Apr. 2020.
- [13] T. Lee, "Collision avoidance for quadrotor UAVs transporting a payload via Voronoi tessellation," in *Proc. Amer. Control Conf.* Chicago, IL, USA: IEEE, Jul. 2015, pp. 1842–1848.
- [14] J. Vicente-Martinez and E. Ramirez-Laboreo, "A hybrid dynamic model and parameter estimation method for accurately simulating overhead cranes with friction," 2025, arXiv preprint 2509.13330.
- [15] M. Fliess, J. Lévine, P. Martin, and P. Rouchon, "Flatness and defect of non-linear systems: introductory theory and examples," *Int. J. Control*, vol. 61, no. 6, pp. 1327–1361, Jun. 1995.
- [16] M. Thomas, T. Werner, and O. Sawodny, "Online trajectory generation and feedforward control for manually-driven cranes with input constraints," in *Proc. IEEE Conf. Control Technol. Appl.*, Aug. 2021, pp. 654–659.
- [17] V. Chung Nguyen, H. Luu Thi, H. Bui Thi Khanh, D. Huy Nguyen, M. N. Vu, and T. Lam Nguyen, "Flatness-Based Motion Planning and Control Strategy of a 3D Overhead Crane," *IEEE Access*, vol. 13, pp. 7053–7070, 2025.
- [18] D. Mellinger and V. Kumar, "Minimum snap trajectory generation and control for quadrotors," in *Proc. IEEE Int. Conf. Robot. Autom.* Shanghai, China: IEEE, May 2011, pp. 2520–2525.
- [19] M. Kelly, "An Introduction to Trajectory Optimization: How to Do Your Own Direct Collocation," *SIAM Review*, vol. 59, no. 4, pp. 849–904, Jan. 2017.
- [20] J. A. E. Andersson, J. Gillis, G. Horn, J. B. Rawlings, and M. Diehl, "CasADi: a software framework for nonlinear optimization and optimal control," *Math. Program. Comput.*, vol. 11, no. 1, pp. 1–36, Mar. 2019.
- [21] A. Wächter and L. T. Biegler, "On the implementation of an interior-point filter line-search algorithm for large-scale nonlinear programming," *Math. Program.*, vol. 106, no. 1, pp. 25–57, Mar. 2006.
- [22] C. Richter, A. Bry, and N. Roy, "Polynomial Trajectory Planning for Aggressive Quadrotor Flight in Dense Indoor Environments," in *Robotics Research*, M. Inaba and P. Corke, Eds. Cham: Springer International Publishing, 2016, vol. 114, pp. 649–666.
- [23] S. Karaman and E. Frazzoli, "Sampling-based algorithms for optimal motion planning," *Int. J. Robot. Res.*, vol. 30, no. 7, pp. 846–894, Jun. 2011.